Simulation of Electromagnetic Scattering of 3-D Inhomogeneous Biaxial Anisotropic Magnetodielectric Objects Embedded in Uniaxial Anisotropic Media by the Mixed-Order BCGS-FFT Method

Jianliang Zhuo, Feng Han, *Member, IEEE*, Longfang Ye, Zhiru Yu, and Qing Huo Liu, *Fellow, IEEE*

***Abstract*— This paper presents a volume integral equation (VIE) solver for the forward electromagnetic scattering of 3-D inhomogeneous biaxial anisotropic objects embedded in uniaxial anisotropic media. The optical axes of the objects can be rotated with arbitrary angles. The mixed-order basis functions are employed to discretize the VIE, i.e., the flux densities ($\boldsymbol{D}$, $\boldsymbol{B}$) are expanded by the volumetric rooftop basis functions and the vector potentials ($\boldsymbol{A}$, $\boldsymbol{F}$) are expanded by the second-order curl conforming basis functions. The weak form of the VIE is formulated by testing it using the same volumetric rooftop basis function and solved by the biconjugate gradient stabilized fast Fourier transform (BCGS-FFT) method. Several numerical simulations of different shapes anisotropic objects are performed and the results are compared with commercial software simulations to validate the accuracy and efficiency of the proposed solver based on different discretization schemes. The major new contribution of this paper is that not only the scatterer but also the background medium is magnetodielectrically anisotropic. Therefore, the dyadic Green's function for the uniaxial anisotropic background medium is evaluated before solving the VIE.**

***Index Terms*— Anisotropic, biconjugate gradient stabilized fast Fourier transform (BCGS-FFT), coupled field volume integral equation (CFVIE), electromagnetic (EM) scattering.**

I. Introduction

In RECENT years, the applications of anisotropic materials have greatly attracted the researchers' interests due to their wide usage for microwaves devices, optical components [1], [2], and aeronautic industry. There are several conventional anisotropic materials. Ferrite is used in microwave devices, such as Faraday rotators, phase shifters, gyrators, and circulators [3]. Liquid crystals are used to design tunable bandpass filters [4], phase shifters [5], and the substrates of the microstrip antennas [6]–[8]. Composite materials based on fibers that display pronounced anisotropy are adopted in aeronautic industry [9]. On the other hand, various novel materials, such as metamaterials [10], [11], nanomaterials [12], and graphene materials [13], also show rapid developments and wide applications.

Since the anisotropic material is widely applied to electromagnetic (EM) devices, its interaction with EM waves, especially the 3-D EM scattering [14]–[16], is of the great concern of researchers. Actually, since the Lorentz–Mie theory that gives the analytical solution of the EM scattering by a uniform anisotropic dielectric sphere [17]–[19], a lot of research work has been done to solve the scattering problems using both analytical and numerical methods [20]–[26]. Geng *et al*. [21] obtain the analytical solution of the 3-D scattering of a plane wave from a uniaxial anisotropic sphere. Dou and Sebak [25] present a generalized 3-D finite-difference time-domain (FDTD) method to model the interaction between EM waves and arbitrary anisotropic media. Cai *et al*. [26] present a linear edge-based finite element method (FEM) for numerical modeling of 3-D controlled-source EM data in an anisotropic conductive medium. Different from FDTD and FEM methods, the integral equation (IE)-based methods [27]–[31] only require the finite computation domain that contains the scatterers to be discretized since Green's function can exactly model the wave propagation from transmitters to scatterers. In the traditional IE-based methods, the method of moment (MOM) [32] is adopted to handle the scattering problems for 3-D anisotropic objects. However, the MOM requires a mass of computation time and memory, especially for electrically large scatterers. Therefore, several fast IE solvers are proposed, such as the multilevel fast multipole algorithm [31], [33], the adaptive integral method [34], the precorrected fast Fourier transform (FFT) method [35], the conjugate gradient fast Fourier transformation method, and the biconjugate gradient FFT method [36]. The

Manuscript received November 30, 2017; revised February 13, 2018 and April 16, 2018; accepted May 4, 2018. Date of publication June 14, 2018; date of current version August 6, 2018. This work was supported by the National Natural Science Foundation of China under Grant 41390453 and Grant 41504120. *(Corresponding authors: Feng Han; Qing Huo Liu.)*

J. Zhuo, F. Han, and L. Ye are with the Institute of Electromagnetics and Acoustics, Xiamen University, Xiamen 361005, China, and also with the Department of Electronic Science, Xiamen University, Xiamen 361005, China (e-mail: feng.han@xmu.edu.cn).

Z. Yu was with the Department of Electrical and Computer Engineering, Duke University, Durham, NC 27708 USA. He is now with the Optical Proximity Correction Group, TSMC Technology, Inc., San Jose, CA 95131 USA.

Q. H. Liu is with the Department of Electrical and Computer Engineering, Duke University, Durham, NC 27708 USA (e-mail: qhliu@duke.edu).

Color versions of one or more of the figures in this paper are available online at http://ieeexplore.ieee.org.

Digital Object Identifier 10.1109/TMTT.2018.2840984

biconjugate gradient stabilized with FFT acceleration (BCGS-FFT) is another commonly used iteration method to solve the large linear systems discretized from the volume IE (VIE) [37]–[40]. Millard and Liu [37] apply the BCGS-FFT method to simulate EM scattering from large inhomogeneous objects embedded in a planarly layered medium. Later, Yu *et al*. [38] present a mixed-order BCGS-FFT method for solving the scattering problem of magnetodielectric objects embedded in the isotropic homogeneous background media. Jia *et al*. [40] further extend this paper to the scattering of magnetodielectric objects with general anisotropy in layered isotropic media.

However, in most of the previous work, the scatterers are embedded in an isotropic medium. In this paper, we consider the anisotropy of the background medium and apply the BCGS-FFT to the 3-D scattering problem for inhomogeneous biaxial anisotropic scatterers with arbitrary shapes embedded in an unbounded uniaxial anisotropic medium. Both the scatterers and the background media have tensor permeability and complex tensor permittivity, and they can be magnetodielectric media with the magnetic contrasts. In addition, mixed-order basis functions of different types are used to expand the flux densities and the vector potentials, i.e., the first-order 3-D volumetric rooftop basis function is used to expand the flux densities, and the second-order curl conforming basis function is used to expand the vector potentials. This paper is an extension of [39], in which the mixed-order basis function and BCGS-FFT method are used to solve the EM scattering problem for anisotropic scatterers embedded in an isotropic medium. In the previous research work dealing with the EM scattering in layered uniaxial media [41], discretized electrical field IE is formulated and several methods, such as the windowing technique and the Padua points, are used to expedite the construction of the impedance matrix. In this paper, we use the mixed-order BCGS-FFT method without the assembly of the impedance matrix to solve the EM scattering of biaxial anisotropic objects embedded in a uniaxial anisotropic background medium. Meanwhile, the optical axis of the scatterer can be rotated with an arbitrary angle. The magnetic and electric vector potentials are employed to formulate the coupled field VIEs (CFVIEs) to weaken the singularity of Green's function in the uniaxial anisotropic media. This method is expected to be very useful and helpful especially for the material engineering, geological prospecting, and biological electromagnetism. Although the whole space is modeled as homogeneous anisotropic in this paper, it may help us understand the EM scattering inside anisotropic media that can be expanded to EM scattering in layered anisotropic media in the future. One possible application of the anisotropic whole space is the detection of objects buried in anisotropic subsurface layers with conductivity attenuation. If the object is far from the layer interfaces, the reflected waves from the interfaces are attenuated by the lossy subsurface medium or they can be time-windowed out, so their effects on the object are negligible. In this situation, it is reasonable to model the subsurface layer as anisotropic whole space to compute the EM scattering. This paper can also provide a reference for the research of scattering problems for more complex anisotropic backgrounds.

The layout of this paper is as follows. In Section II, the CFVIE for anisotropic scatterers embedded in an anisotropic background medium is given and its weak form is obtained by the mixed-order basis function expansion and volumetric rooftop function testing. In Section III, four numerical examples for EM scattering by inhomogeneous anisotropic objects with different shapes are shown to validate the accuracy and performance of our method. And in Section IV, conclusions are drawn and some critical achievements of this paper are discussed.

II. Formulation

The objective of this paper is to solve the scattering problem of inhomogeneous biaxial anisotropic magnetodielectric objects embedded in an unbounded uniaxial anisotropic background medium with the optic axis in the z-direction. The time dependence $e^{j\omega t}$ is used throughout this paper. The permeability tensor $\overline{\overline{\mu}}_b$ and the complex permittivity tensor $\overline{\overline{\epsilon}}_b$ of the background medium are

$$\overline{\overline{\mu}}_b = \begin{bmatrix} \mu_{xb} & 0 & 0 \\ 0 & \mu_{xb} & 0 \\ 0 & 0 & \mu_{zb} \end{bmatrix} \quad \overline{\overline{\epsilon}}_b = \begin{bmatrix} \epsilon_{xb} & 0 & 0 \\ 0 & \epsilon_{xb} & 0 \\ 0 & 0 & \epsilon_{zb} \end{bmatrix} \tag{1}$$

where $\overline{\overline{\epsilon}}_b$ is defined as

$$\overline{\overline{\epsilon}}_b = \overline{\overline{\varepsilon}}_b + \frac{\overline{\overline{\sigma}}_b}{j\omega}. \tag{2}$$

The parameter $\overline{\overline{\varepsilon}}_b$ is the dielectric constant tensor and $\overline{\overline{\sigma}}_b$ is the conductivity tensor. They can be written as

$$\overline{\overline{\varepsilon}}_b = \begin{bmatrix} \varepsilon_{xb} & 0 & 0 \\ 0 & \varepsilon_{xb} & 0 \\ 0 & 0 & \varepsilon_{zb} \end{bmatrix} \quad \overline{\overline{\sigma}}_b = \begin{bmatrix} \sigma_{xb} & 0 & 0 \\ 0 & \sigma_{xb} & 0 \\ 0 & 0 & \sigma_{zb} \end{bmatrix}. \tag{3}$$

And the permeability tensor $\overline{\overline{\mu}}_s$ and the complex permittivity tensor $\overline{\overline{\epsilon}}_s$ of the scatterers are assumed to be

$$\overline{\overline{\mu}}_s = \begin{bmatrix} \mu_{xs} & 0 & 0 \\ 0 & \mu_{ys} & 0 \\ 0 & 0 & \mu_{zs} \end{bmatrix} \quad \overline{\overline{\epsilon}}_s = \begin{bmatrix} \epsilon_{xs} & 0 & 0 \\ 0 & \epsilon_{ys} & 0 \\ 0 & 0 & \epsilon_{zs} \end{bmatrix} \tag{4}$$

where $\overline{\overline{\epsilon}}_s$ contains information about the dielectric constant tensor $\overline{\overline{\varepsilon}}_s$ and conductivity tensor $\overline{\overline{\sigma}}_s$.

A. Coupled Field Volume Integral Equations

According to the volume equivalence principle [42], the electric field $\mathbf{E}^s$ and magnetic fields $\mathbf{H}^s$ scattered form the objects are equal to the fields radiated by the equivalent electric current source $\mathbf{J}_{\text{eq}}$ and the magnetic current source $\mathbf{M}_{\text{eq}}$ inside the anisotropic objects. They can be expressed as

$$\mathbf{J}_{\text{eq}}(\mathbf{r}) = j\omega\overline{\overline{\chi}}_{\epsilon}(\mathbf{r})\mathbf{D}(\mathbf{r}) \tag{5}$$

$$\mathbf{M}_{\text{eq}}(\mathbf{r}) = j\omega\overline{\overline{\chi}}_{\mu}(\mathbf{r})\mathbf{B}(\mathbf{r}) \tag{6}$$

where the tensor

$$\overline{\overline{\chi}}_{\epsilon}(\mathbf{r}) = [\overline{\overline{\epsilon}}(\mathbf{r}) - \overline{\overline{\epsilon}}_b]\overline{\overline{\epsilon}}^{-1}(\mathbf{r}) \tag{7}$$

is the dielectric contrast function, and the tensor

$$\overline{\overline{\chi}}_{\mu}(\mathbf{r}) = [\overline{\overline{\mu}}(\mathbf{r}) - \overline{\overline{\mu}}_b]\overline{\overline{\mu}}^{-1}(\mathbf{r}) \tag{8}$$

is the magnetic contrast function. $\overline{\overline{\mu}}(\mathbf{r})$ and $\overline{\overline{\epsilon}}(\mathbf{r})$ are permeability tensor and complex permittivity tensor at any point $\mathbf{r}$ in the whole space. When $\mathbf{r}$ is located inside the scatterer, $\overline{\overline{\mu}}(\mathbf{r})$ and $\overline{\overline{\epsilon}}(\mathbf{r})$ are equal to the dielectric parameters of the scatterer but equal to the background dielectric parameters if $\mathbf{r}$ is located outside the scatterer. $\mathbf{D} = \overline{\overline{\epsilon}}\mathbf{E}$ and $\mathbf{B} = \overline{\overline{\mu}}\mathbf{H}$ are the total electric and magnetic flux densities, respectively. It is easy to formulate CFVIE as

$$\mathbf{E}^i(\mathbf{r}) = \overline{\overline{\epsilon}}^{-1}(\mathbf{r})\mathbf{D}(\mathbf{r}) + j\omega\left[\mathbf{I} + \frac{\nabla\nabla\cdot\overline{\overline{\epsilon}}_b}{\omega^2\tau_\epsilon}\right]\mathbf{A}(\mathbf{r}) + \overline{\overline{\epsilon}}_b^{-1}\nabla\times\mathbf{F}(\mathbf{r}) \tag{9}$$

$$\mathbf{H}^i(\mathbf{r}) = \overline{\overline{\mu}}^{-1}(\mathbf{r})\mathbf{B}(\mathbf{r}) + j\omega\left[\mathbf{I} + \frac{\nabla\nabla\cdot\overline{\overline{\mu}}_b}{\omega^2\tau_\mu}\right]\mathbf{F}(\mathbf{r}) - \overline{\overline{\mu}}_b^{-1}\nabla\times\mathbf{A}(\mathbf{r}) \tag{10}$$

where $\tau_\epsilon = \mu_{zb}\epsilon_{zb}^2$ and $\tau_\mu = \mu_{zb}^2\epsilon_{zb}$ are the gauges for the anisotropic media suggested by Chew [43], and the magnetic and electric vector potentials $\mathbf{A}$ and $\mathbf{F}$ are given as

$$\mathbf{A}(\mathbf{r}) = j\omega\int_V \overline{\overline{\mathbf{G}}}_{\mathbf{AJ}}(\mathbf{r},\mathbf{r}')\overline{\overline{\chi}}_\epsilon(\mathbf{r}')\mathbf{D}(\mathbf{r}')d\mathbf{r}' \tag{11}$$

$$\mathbf{F}(\mathbf{r}) = j\omega\int_V \overline{\overline{\mathbf{G}}}_{\mathbf{FM}}(\mathbf{r},\mathbf{r}')\overline{\overline{\chi}}_\mu(\mathbf{r}')\mathbf{B}(\mathbf{r}')d\mathbf{r}' \tag{12}$$

where $\overline{\overline{\mathbf{G}}}_{\mathbf{AJ}}(\mathbf{r},\mathbf{r}')$ and $\overline{\overline{\mathbf{G}}}_{\mathbf{FM}}(\mathbf{r},\mathbf{r}')$ are the dyadic Green's function (DGF) of the electric vector potential $\mathbf{A}$ (DGFA) and the DGF of the electric vector potential $\mathbf{F}$ (DGFF) for the background medium. $\mathbf{r}$ is the observation (field) point and $\mathbf{r}'$ is the source point. As unknowns of (9) and (10), $\mathbf{D}$ and $\mathbf{B}$ are solved by the BCGS-FFT method to obtain the fields anywhere in the whole space. Therefore, in virtue of (5) and (6), the scattered electric and magnetic field at any point $\mathbf{r}$ can obtained as

$$\mathbf{E}^s(\mathbf{r}) = \int_V \overline{\overline{\mathbf{G}}}_{\mathbf{EJ}}(\mathbf{r},\mathbf{r}')\mathbf{J}_{\text{eq}}(\mathbf{r}')d\mathbf{r}' + \int_V \overline{\overline{\mathbf{G}}}_{\mathbf{EM}}(\mathbf{r},\mathbf{r}')\mathbf{M}_{\text{eq}}(\mathbf{r}')d\mathbf{r}' \tag{13}$$

$$\mathbf{H}^s(\mathbf{r}) = \int_V \overline{\overline{\mathbf{G}}}_{\mathbf{HM}}(\mathbf{r},\mathbf{r}')\mathbf{M}_{\text{eq}}(\mathbf{r}')d\mathbf{r}' + \int_V \overline{\overline{\mathbf{G}}}_{\mathbf{HJ}}(\mathbf{r},\mathbf{r}')\mathbf{J}_{\text{eq}}(\mathbf{r}')d\mathbf{r}' \tag{14}$$

where $\overline{\overline{\mathbf{G}}}_{\mathbf{EJ}}(\mathbf{r},\mathbf{r}')$ and $\overline{\overline{\mathbf{G}}}_{\mathbf{HJ}}(\mathbf{r},\mathbf{r}')$ are DGFs relating the electric current $\mathbf{J}$ at the source point $\mathbf{r}'$ to the electric and magnetic field at the field point $\mathbf{r}$, respectively. The detailed derivations of $\overline{\overline{\mathbf{G}}}_{\mathbf{EJ}}$ and $\overline{\overline{\mathbf{G}}}_{\mathbf{HJ}}$ in uniaxial anisotropic media can be found in [44] and are also summarized briefly in Appendix A. Similarly, $\overline{\overline{\mathbf{G}}}_{\mathbf{EM}}(\mathbf{r},\mathbf{r}')$ and $\overline{\overline{\mathbf{G}}}_{\mathbf{HM}}(\mathbf{r},\mathbf{r}')$ are DGFs relating the magnetic current $\mathbf{M}$ at the source point $\mathbf{r}'$ to the electric and magnetic field at the field point $\mathbf{r}$, respectively, and their expressions can be obtained from $\overline{\overline{\mathbf{G}}}_{\mathbf{HJ}}(\mathbf{r},\mathbf{r}')$ and $\overline{\overline{\mathbf{G}}}_{\mathbf{EJ}}(\mathbf{r},\mathbf{r}')$ by the duality theory.

B. Dyadic Green's Functions of the Vector Potentials in Uniaxial Anisotropic Media

The magnetic vector potential $\mathbf{A}$ is related to the equivalent current density through Green's function, i.e., the scalar Green's function for the homogeneous media and the DGF for the layered media or the anisotropic media. The DGFs of the vector potential are the kernel of MOM for solving the VIEs. Although, in [44], the analytic expressions of the $\overline{\overline{\mathbf{G}}}_{\mathbf{EJ}}$ and $\overline{\overline{\mathbf{G}}}_{\mathbf{HJ}}$ are given, it is difficult to obtain the analytic expressions for $\overline{\overline{\mathbf{G}}}_{\mathbf{AJ}}$ and $\overline{\overline{\mathbf{G}}}_{\mathbf{FM}}$ following the similar procedure. Therefore, we use the method of wave decomposition in the spectral domain to evaluate $\overline{\overline{\mathbf{G}}}_{\mathbf{AJ}}$ and $\overline{\overline{\mathbf{G}}}_{\mathbf{FM}}$ through the Sommerfeld integration [45].

When the observation (field) point $\mathbf{r} = \hat{\mathbf{x}}x + \hat{\mathbf{y}}y + \hat{\mathbf{z}}z$ and the source point $\mathbf{r}' = \hat{\mathbf{x}}x' + \hat{\mathbf{y}}y' + \hat{\mathbf{z}}z'$ are located in different positions, the computation of DGFA in the uniaxial anisotropic medium [45] is shown as

$$\overline{\overline{\mathbf{G}}}_{\mathbf{AJ}}(\mathbf{r},\mathbf{r}') = \frac{1}{(2\pi)^3}\iiint_{-\infty}^{+\infty}\frac{\overline{\overline{Z}}_A^a}{|\overline{\overline{Z}}_A|}e^{-j\mathbf{k}\cdot(\mathbf{r}-\mathbf{r}')}d\mathbf{k} \tag{15}$$

where the subscript $\mathbf{J}$ means that the DGFA is corresponding to the electric current $\mathbf{J}_{\text{eq}}$. $\mathbf{k}$ is the wave vector and $\overline{\overline{Z}}_A^a$ is the adjoint matrix of $\overline{\overline{Z}}_A$ whose determinant is $|\overline{\overline{Z}}_A|$. $\overline{\overline{Z}}_A$ is the electric wave matrix about (k_x, k_y, k_z), whose derivation and the complete expression are given in [45]. Based on Cauchy's residue theorem and several mathematical identities, (15) is finally simplified to the Sommerfeld integrals, and the derivation details can be found in [45].

However, when the discretized CFVIE is solved, we need to compute the contribution of the equivalent current to the values of $\mathbf{A}$ at all the discretized cells. Equation (15) is used to compute the DGFAs when the cell in which the equivalent current locates differs from the cell in which $\mathbf{A}$ is evaluated, i.e., when $\mathbf{r}'$ and $\mathbf{r}$ are not overlapped. But when the two cells are the same, i.e., $\mathbf{r}'$ and $\mathbf{r}$ are overlapped, (15) cannot be directly used to evaluate the DGFA due to the singularity. In an isotropic background medium, the mean DGFA is evaluated analytically to handle this singularity [34]. However, in anisotropic media, there is no explicit expression for the mean DGFA. The numerical average value is used. It is assumed that observation point $\mathbf{r}$ is located in the center of the cell, and we uniformly discretize it to several smaller cells and put the equivalent current source points $\mathbf{r}'$ in the centers of these smaller cells. The DGFA for each source point is evaluated using (15), and the final average value of the DGFAs for all the smaller cells is the mean DGFA.

According to the duality theory, it is easy to obtain the DGFF that is corresponding to the equivalent magnetic current.

C. Discretization of Mixed-Order Expansions

Discretization is the essential process for solving (9) and (10) by the BCGS-FFT method. From (11) and (12), we know that the unknowns of the vector potentials ($\mathbf{A}$ and $\mathbf{F}$) depend on the unknowns of the flux densities ($\mathbf{D}$ and $\mathbf{B}$). Thus, the flux densities ($\mathbf{D}$ and $\mathbf{B}$) are the only couple independent unknowns. Although expanding flux densities could satisfy the needs of solving (9) and (10), the previous work [38], [39] suggests that expanding vector potentials can help weakening the singularities of the IEs. Therefore, in this paper, the first-order 3-D volumetric rooftop basis function is used to expand the flux densities, and the second-order curl conforming basis

function is used to expand vector potentials (**A** and **F**) to preserve the continuity of these physical variables in the boundaries.

Several shapes of cell elements can be used to discretize the computation domain. However, the interaction between equivalent sources and DGFs is actually the operation of convolution [38]. Therefore, in this paper, cubic cells are adopted to facilitate the FFT acceleration of the convolution.

All scatterers are completely embedded in a rectangular computation domain D that is discretized into $I_1 \times I_2 \times I_3$ uniform cubic cells with the dimension of $\triangle x$. Let $i_1 \in [1, I_1]$, $i_2 \in [1, I_2]$, $i_3 \in [1, I_3]$, and the center location $\mathbf{r_i}$ of any cell $\mathbf{i} = \{i_1, i_2, i_3\}$ is given by

$$\mathbf{r_i} = \sum_{q=1}^{3} \hat{x}_q \left(i_q - \frac{1}{2} \right) \triangle x \tag{16}$$

where $\{\hat{x}_1, \hat{x}_2, \hat{x}_3\} = \{\hat{x}, \hat{y}, \hat{z}\}$. If a cell is small enough, the permittivity tensor $\overline{\overline{\epsilon}}_{\mathbf{i}}$ and permeability tensor $\overline{\overline{\mu}}_{\mathbf{i}}$ are considered as constants with the values depending on the center location $\mathbf{r_i}$.

In this paper, the flux densities (**D** and **B**) are expanded by the 3-D volumetric rooftop basis functions. And the expansions are given as

$$\mathbf{D}^{(q)}(\mathbf{r}) = \sum_{\mathbf{i}} d_{\mathbf{i}}^{(q)} \Psi_{\mathbf{i}}^{(q)}(\mathbf{r}) \tag{17}$$

$$\mathbf{B}^{(q)}(\mathbf{r}) = \sum_{\mathbf{i}} b_{\mathbf{i}}^{(q)} \Psi_{\mathbf{i}}^{(q)}(\mathbf{r}) \tag{18}$$

where $d_{\mathbf{i}}^{(q)}$ and $b_{\mathbf{i}}^{(q)}$ are the expansion coefficients for $\mathbf{D}^{(q)}$ and $\mathbf{B}^{(q)}$, and $q \in \{1, 2, 3\}$. The detailed expression of the basis function $\Psi_i^{(q)}(\mathbf{r})$ can be found in [39].

Because of the continuity boundary conditions of the vector potentials and existence of the curl operation in (9) and (10) [38], [39], the 3-D second-order curl conforming basis function $\Phi_{\mathbf{i};\mathbf{m}}^{(q)}(\mathbf{r_i})$ is selected to expand the magnetic and electric vector potentials **A** and **F**

$$\mathbf{A}^{(q)}(\mathbf{r}) = \sum_{\mathbf{i}} \sum_{\mathbf{m}} a_{\mathbf{i};\mathbf{m}}^{(q)} \Phi_{\mathbf{i};\mathbf{m}}^{(q)}(\mathbf{r}) \tag{19}$$

$$\mathbf{F}^{(q)}(\mathbf{r}) = \sum_{\mathbf{i}} \sum_{\mathbf{m}} f_{\mathbf{i};\mathbf{m}}^{(q)} \Phi_{\mathbf{i};\mathbf{m}}^{(q)}(\mathbf{r}) \tag{20}$$

where $a_{\mathbf{i};\mathbf{m}}^{(q)}$ and $f_{\mathbf{i};\mathbf{m}}^{(q)}$ are the expansion coefficients for $\mathbf{A}^{(q)}$ and $\mathbf{F}^{(q)}$, and $q \in \{1, 2, 3\}$. $\mathbf{m}$ is the node point index of curl conforming basis functions within one cell, and the node location is given by

$$\mathbf{r}_{\mathbf{i};\mathbf{m}}^{(q)} = \mathbf{r_i} + \hat{x}_q (-1)^{m_q} \frac{\triangle x_q}{2} + \sum_{n=1}^{2} \hat{x}_{q+n} \frac{m_{q+n} - 2}{2} \triangle x_{q+n} \tag{21}$$

where $\mathbf{m} = \{m_1, m_2, m_3\}$, $m_1 = \{1, 2\}$, and $m_{2,3} = \{1, 2, 3\}$. More details of the 3-D second-order curl conforming basis function are presented in [38] and [39].

According to (11) and (12), $a_{\mathbf{i};\mathbf{m}}^{(q)}$ and $f_{\mathbf{i};\mathbf{m}}^{(q)}$ are formulated as

$$a_{\mathbf{i};\mathbf{m}}^{(q)} = j\omega \sum_{\mathbf{K}} \sum_{s=1}^{3} g_{a,qs}\left(\mathbf{r}_{\mathbf{i};\mathbf{m}}^{(q)}, \mathbf{r}_{\mathbf{K}}^{(q)}\right) \sum_{l=1}^{3} \chi'_{\epsilon,sl}\left(\mathbf{r}_{\mathbf{K}}^{(q)}\right) d_{\mathbf{K}}^{(l)} \tag{22}$$

$$f_{\mathbf{i};\mathbf{m}}^{(q)} = j\omega \sum_{\mathbf{K}} \sum_{s=1}^{3} g_{f,qs}\left(\mathbf{r}_{\mathbf{i};\mathbf{m}}^{(q)}, \mathbf{r}_{\mathbf{K}}^{(q)}\right) \sum_{l=1}^{3} \chi'_{\mu,sl}\left(\mathbf{r}_{\mathbf{K}}^{(q)}\right) b_{\mathbf{K}}^{(l)} \tag{23}$$

where $\mathbf{K} = \{k_1, k_2, k_3\}$, $k_1 \in [1, I_1 + 1]$, $k_2 \in [1, I_2 + 1]$, and $k_3 \in [1, I_3 + 1]$, and q, s, $l = \{1, 2, 3\}$. $\mathbf{r}_{\mathbf{K}}^{(q)}$ is the location of equivalent source point for each cell. $g_{a,qs}$ and $g_{f,qs}$ are the qs component of DGFA and DGFF, respectively. They are evaluated according to (15) when $\mathbf{r}_{\mathbf{i};\mathbf{m}}^{(q)} \neq \mathbf{r}_{\mathbf{K}}^{(q)}$, but the mean DGFs are used when $\mathbf{r}_{\mathbf{i};\mathbf{m}}^{(q)} = \mathbf{r}_{\mathbf{K}}^{(q)}$. $\chi'_{\epsilon,sl}$ and $\chi'_{\mu,sl}$ are the sl components of the discrete contrast function that is defined as

$$\overline{\overline{\chi}}'_{\eta}\left(\mathbf{r}_{\mathbf{K}}^{(q)}\right) = \frac{\overline{\overline{\chi}}_{\eta}(\mathbf{r}_{\mathbf{K}} - \hat{x}_q \triangle x_q) + \overline{\overline{\chi}}_{\eta}(\mathbf{r}_{\mathbf{K}})}{2} \tag{24}$$

where $\eta = \epsilon$ or μ. In this paper, FFT is used to accelerate the convolution in (22) and (23).

D. Weak Form CFVIE

Using the 3-D volumetric rooftop basis functions $\Psi_i^{(p)}(\mathbf{r})$ to test the strong form CFVIE in (9) and (10), we can obtain the weak form CFVIE

$$\begin{aligned} e_{\mathbf{i}}^{\mathrm{inc},(p)} = & \int_V \Psi_i^{(p)}(\mathbf{r}) \cdot \overline{\overline{\epsilon}}^{-1}(\mathbf{r}) \mathbf{D}(\mathbf{r}) d\mathbf{r} \\ & + j\omega \int_V \Psi_i^{(p)}(\mathbf{r}) \cdot \left[\mathbf{I} + \frac{\nabla\nabla \cdot \overline{\overline{\epsilon}}_b}{\omega^2 \tau_\epsilon} \right] \mathbf{A}(\mathbf{r}) d\mathbf{r} \\ & + \overline{\overline{\epsilon}}_b^{-1} \int_V \Psi_i^{(p)}(\mathbf{r}) \cdot \nabla \times \mathbf{F}(\mathbf{r}) d\mathbf{r} \end{aligned} \tag{25}$$

$$\begin{aligned} h_{\mathbf{i}}^{\mathrm{inc},(p)} = & \int_V \Psi_i^{(p)}(\mathbf{r}) \cdot \overline{\overline{\mu}}^{-1}(\mathbf{r}) \mathbf{B}(\mathbf{r}) d\mathbf{r} \\ & + j\omega \int_V \Psi_i^{(p)}(\mathbf{r}) \cdot \left[\mathbf{I} + \frac{\nabla\nabla \cdot \overline{\overline{\mu}}_b}{\omega^2 \tau_\mu} \right] \mathbf{F}(\mathbf{r}) d\mathbf{r} \\ & - \overline{\overline{\mu}}_b^{-1} \int_V \Psi_i^{(p)}(\mathbf{r}) \cdot \nabla \times \mathbf{A}(\mathbf{r}) d\mathbf{r} \end{aligned} \tag{26}$$

where $p = \{1, 2, 3\}$, and

$$e_{\mathbf{i}}^{\mathrm{inc},(p)} = \int_V \Psi_i^{(p)}(\mathbf{r}) \cdot \mathbf{E}(\mathbf{r}) d\mathbf{r} \tag{27}$$

$$h_{\mathbf{i}}^{\mathrm{inc},(p)} = \int_V \Psi_i^{(p)}(\mathbf{r}) \cdot \mathbf{H}(\mathbf{r}) d\mathbf{r}. \tag{28}$$

Substituting (17)–(23) into (25) and (26), we obtain the weak form CFIVE

$$\begin{aligned} & e_{\mathbf{i}}^{\mathrm{inc},(p)} \\ & = \sum_{q=p}^{p+2} \sum_{l=1}^{3} S_{\overline{\overline{\epsilon}},q,\mathbf{i}}^{(q)} d_{\mathbf{i}-\hat{x}_p(2-l)}^{(q)} + j\omega \frac{\triangle V}{8} \\ & \quad \times \sum_{Z=1}^{2} \sum_{\mathbf{m}} \left\{ a_{\mathbf{i}-\hat{x}_p(2-Z);\mathbf{m}}^{(p)} \frac{1 + \delta_{m_q,(3-Z)}}{3} \right. \\ & \qquad \left. \times V(m_{q+1}) V(m_{q+2}) - \frac{2}{k_{bz} \triangle x_p} \sum_q \frac{\epsilon_{qb}}{\epsilon_{zb}} \frac{(-1)^{z+1}}{\triangle x_q} \right. \end{aligned}$$

$$\times(-1)^{m_q}a^{(p)}_{\mathbf{i}-\hat{x}_p(2-Z);\mathbf{m}}V(m_{q+1})V(m_{q+2}) + \frac{1}{j\omega\epsilon_{pb}}\left[\frac{2}{\triangle x_{p+1}}f^{(p+2)}_{\mathbf{i}-\hat{x}_p(2-Z);\mathbf{m}}T(m_p,Z) \times R(m_{p+1}) - \frac{2}{\triangle x_{p+2}}f^{(p+1)}_{\mathbf{i}-\hat{x}_p(2-Z);\mathbf{m}} \times T(m_p,Z)R(m_{p+2})\right]\Bigg\} \tag{29}$$

$$h^{\mathrm{inc},(p)}_{\mathbf{i}} = \sum_{q=p}^{p+2}\sum_{l=1}^{3}S^{(q)}_{\overline{\overline{\mu}},q,\mathbf{i}}d^{(q)}_{\mathbf{i}-\hat{x}_p(2-l)} + j\omega\frac{\triangle V}{8} \times\sum_{Z=1}^{2}\sum_{\mathbf{m}}\Bigg\{f^{(p)}_{\mathbf{i}-\hat{x}_p(2-Z);\mathbf{m}}\frac{1+\delta_{m_q,(3-Z)}}{3} \times V(m_{q+1})V(m_{q+2}) - \frac{2}{k_{bz}\triangle x_p} \times\sum_{q}\frac{\mu_{qb}}{\mu_{zb}}\frac{(-1)^{z+1}}{\triangle x_q} \times(-1)^{m_q}f^{(p)}_{\mathbf{i}-\hat{x}_p(2-Z);\mathbf{m}}V(m_{q+1})V(m_{q+2}) - \frac{1}{j\omega\mu_{pb}}\left[\frac{2}{\triangle x_{p+1}}a^{(p+2)}_{\mathbf{i}-\hat{x}_p(2-Z);\mathbf{m}} \times T(m_p,Z)R(m_{p+1} - \frac{2}{\triangle x_{p+2}} \times a^{(p+1)}_{\mathbf{i}-\hat{x}_p(2-Z);\mathbf{m}}T(m_p,Z)R(m_{p+2})\right]\Bigg\} \tag{30}$$

where $k_{zb} = (\omega^2\epsilon_{zb}\mu_{zb})^{1/2}$, $p = \{1, 2, 3\}$

$$V = \left\{\frac{1}{3}\quad\frac{4}{3}\quad\frac{1}{3}\right\} \tag{31}$$

$$R = \{-1\quad 0\quad 1\} \tag{32}$$

$$T = \begin{Bmatrix}0 & \frac{1}{3}\\ \frac{2}{3} & \frac{2}{3}\\ \frac{1}{3} & 0\end{Bmatrix}. \tag{33}$$

And p and q are the cyclic indexes with the period of 3. When $q = p$

$$S^{(q)}_{\eta,\mathbf{i}} = \frac{\triangle V}{6}\begin{Bmatrix}\eta^{-1}_{\mathbf{i}-\hat{x}_p,pp}\\ 2\eta^{-1}_{\mathbf{i}-\hat{x}_p,pp}+2\eta^{-1}_{\mathbf{i},pp}\\ \eta^{-1}_{\mathbf{i},pp}\end{Bmatrix} \tag{34}$$

where $\eta^{-1}_{\mathbf{i},pp}$ is pp component of the inverse matrix η, $\eta = \overline{\overline{\epsilon}}$ or $\overline{\overline{\mu}}$. When $q = p+1$ or $q = p+2$

$$S^{(q)}_{\eta,\mathbf{i}} = \frac{\triangle V}{4}\begin{Bmatrix}\eta^{-1}_{\mathbf{i}-\hat{x}_p,pq}\\ \eta^{-1}_{\mathbf{i},pq}\\ 0\end{Bmatrix}. \tag{35}$$

In (29) and (30), the unknown coefficients $d^{(p)}_i$ and $b^{(p)}_i$ are solved by the BCGS iteration. In each iteration, the coefficients $a^{(p)}_{i;m}$ and $f^{(p)}_{i;m}$ are computed by the convolution between $d^{(p)}_i$ and $b^{(p)}_i$ and DGFA and DGFF, respectively, which are actually accelerated by FFT.

III. Numerical Results

It is easy to find that the aforementioned formulation is suitable for arbitrary 3-D anisotropic magnetodielectric objects. In addition, an arbitrary 3-D shape can be assembled from a variety of canonical 3-D shapes, such as cube, cylinder, and sphere. In fact, this is the way the available commercial software currently works. Therefore, in this section, we design there canonical 3-D shapes to validate the method shown in Section II, and the BCGS-FFT results are compared with the simulation results from the commercial FEM software COMSOL. For convenience, several basic parameters are set the same, and they are no longer repeated for each case. The background parameters shown in (1) and (3) are set as $\mu_{xb} = \mu_0$, $\mu_{zb} = 2\mu_0$, $\varepsilon_{xb} = \varepsilon_0$, $\varepsilon_{zb} = 2\varepsilon_0$, $\sigma_{xb} = 10^{-3}$ S/m, and $\sigma_{zb} = 2\times10^{-3}$ S/m. The source is a unit electric dipole, operating at 1 GHz and polarized by (1, 1, 1). The rectangular coordinate is used for all cases, and the origin coincides with the center of the scatterer. The EM scattering of several typical objects are demonstrated latter. All cases and COMSOL simulations are performed on a workstation with 20-cores Xeon E2650 v3 2.3-GHz CPU and 512-GB RAM.

A. Two-Layered Biaxial Anisotropic Cube

The scatterer is a two-layered cube with the size of 0.4 m × 0.4 m × 0.4 m, as shown in Fig. 1. Two layers have the same thickness 0.2 m. And the permittivity tensors and permeability tensors are

$$\overline{\overline{\mu}}_{s1} = \mu_0\begin{bmatrix}2.0 & 0 & 0\\ 0 & 0.75 & 0\\ 0 & 0 & 2.5\end{bmatrix}\quad\overline{\overline{\mu}}_{s2} = \mu_0\begin{bmatrix}0.7 & 0 & 0\\ 0 & 1.5 & 0\\ 0 & 0 & 3.0\end{bmatrix} \tag{36}$$

$$\overline{\overline{\varepsilon}}_{s1} = \varepsilon_0\begin{bmatrix}0.8 & 0 & 0\\ 0 & 1.6 & 0\\ 0 & 0 & 3.0\end{bmatrix}\quad\overline{\overline{\varepsilon}}_{s2} = \varepsilon_0\begin{bmatrix}1.5 & 0 & 0\\ 0 & 0.8 & 0\\ 0 & 0 & 3.0\end{bmatrix} \tag{37}$$

$$\overline{\overline{\sigma}}_{s1} = \overline{\overline{\sigma}}_{s2} = \begin{bmatrix}0.01 & 0 & 0\\ 0 & 0.02 & 0\\ 0 & 0 & 0.03\end{bmatrix}\ \text{S/m}. \tag{38}$$

The source is located at $(0, 0, -0.25)$ m. The receiver array consists of 40 receivers and is located at the $z = 0.25$ m plane. The computation domain has the same size as that of the scatterer, and two different discretization schemes, which are 10 points per wavelength (PPW) and 25 PPW, are chosen to show the performance of the proposed method. The computation domain is discretized into 40^3 cells by 10 PPW with 36.4 thousand unknowns and 100^3 cells by 25 PPW with 6 million unknowns. In the COMSOL simulation model, the computation domain is 0.6 m × 0.6 m × 0.6 m which includes the electric dipole source, and the thickness of the perfect match layers (PMLs) is set as 0.05 m on the periphery of the computation domain. In order to maintain the COMSOL

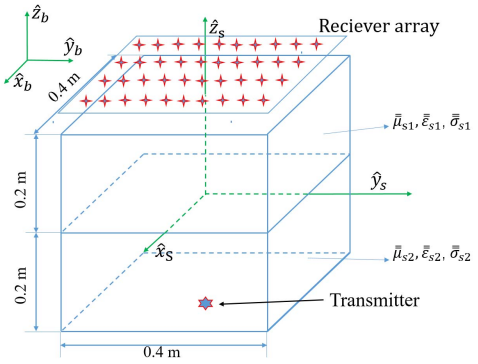

Fig. 1. Geometry of a two-layered cubic scatterer with the dimension of 0.4 m × 0.4 m × 0.4 m.

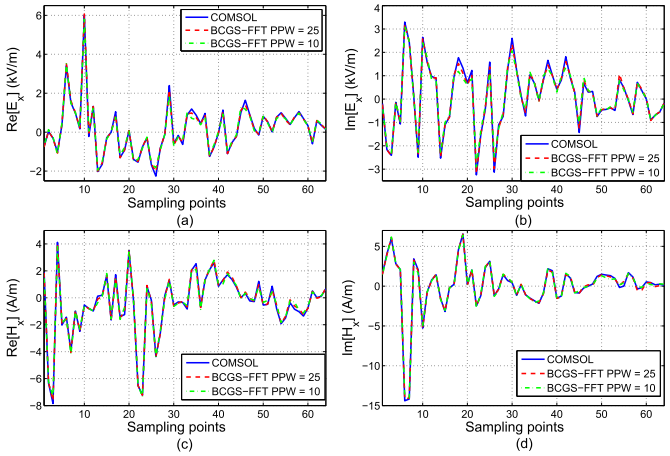

Fig. 2. x-component comparisons of the total fields inside the two-layered cubic scatterer by the mixed-order BCGS-FFT and COMSOL. (a) and (b) Real and imaginary parts of the electric fields, respectively. (c) and (d) Real and imaginary parts of the magnetic fields, respectively.

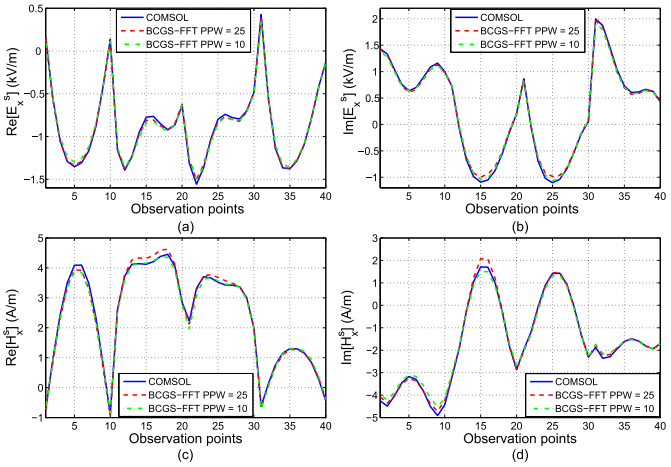

Fig. 3. x-component comparisons of the scattered fields at receiver array by the mixed-order BCGS-FFT and COMSOL. (a) and (b) Real and imaginary parts of the electric fields, respectively. (c) and (d) Real parts and imaginary parts of the magnetic fields, respectively.

simulation accuracy, the mesh sizes are set to be "EXTRA FINE." The mesh sizes and PML settings are the same for all the COMSOL simulations presented in this paper. Fig. 2 shows the comparisons of the total fields inside the anisotropic object solved by our BCGS-FFT method and COMSOL simulations, whereas Fig. 3 shows the comparisons of scattered fields at the receiver array. Here, we only pick 64 uniformly distributed sampling points inside the anisotropic object for the total field comparisons. We can see that the x-components of both the total fields and scattered fields by our BCGS-FFT method match the COMSOL simulated results well. Other components also have the same good agreements and are not shown here. By treating the COMSOL simulated results as reference, we quantitatively compare our results with the reference. For the computed total fields, the relative error is 12.8% when PPW = 10 and decreases to 6.3% when PPW = 25. For the scattered fields, the relative error is 5.0% when PPW = 10 and decreases to 4.1% when PPW = 25. It is obvious that the higher accuracy is achieved when PPW is larger. In this case, the required time of the total calculation process is 52 s for PPW = 10 and 338 s for PPW = 25. The memory consumption is 1 GB for PPW = 10 and 10 GB for PPW = 25. COMSOL requires 2363 s and 86-GB memory on the same machine.

B. Two-Layered Biaxial Anisotropic Cylinder

In this case, a two-layered concentric cylindrical scatterer is considered. The geometry of the scatterer is shown in Fig. 4. It has the inner radius $r_1 = 0.1$ m, the outer radius $r_2 = 0.2$ m, and the height $h = 0.4$ m. And the permittivity tensors and permeability tensors are given as

$$\overline{\overline{\mu}}_{s1} = \mu_0 \begin{bmatrix} 1.5 & 0 & 0 \\ 0 & 2.0 & 0 \\ 0 & 0 & 3.0 \end{bmatrix} \quad \overline{\overline{\varepsilon}}_{s1} = \varepsilon_0 \begin{bmatrix} 2.0 & 0 & 0 \\ 0 & 1.5 & 0 \\ 0 & 0 & 3.0 \end{bmatrix} \tag{39}$$

$$\overline{\overline{\sigma}}_{s1} = \begin{bmatrix} 0.02 & 0 & 0 \\ 0 & 0.015 & 0 \\ 0 & 0 & 0.03 \end{bmatrix} \text{ S/m} \tag{40}$$

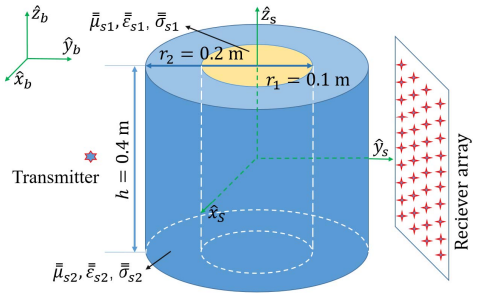

Fig. 4. Geometry of a two-layered concentric cylindrical scatterer with the radii $r_1 = 0.1$ m and $r_2 = 0.2$ m and the height of $h = 0.4$ m.

for the internal cylinder, and

$$\overline{\overline{\mu}}_{s2} = \mu_0 \begin{bmatrix} 2.0 & 0 & 0 \\ 0 & 1.5 & 0 \\ 0 & 0 & 3.0 \end{bmatrix} \quad \overline{\overline{\varepsilon}}_{s2} = \varepsilon_0 \begin{bmatrix} 1.5 & 0 & 0 \\ 0 & 2.0 & 0 \\ 0 & 0 & 2.5 \end{bmatrix} \tag{41}$$

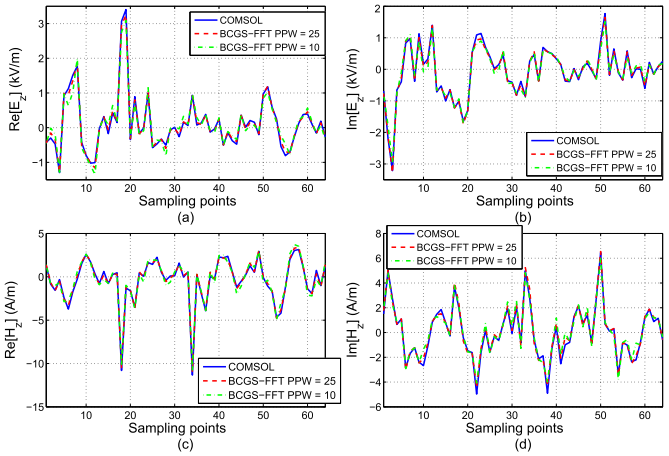

Fig. 5. z-component comparisons of the total fields inside the two-layered concentric cylindrical scatterer by the mixed-order BCGS-FFT and COMSOL. (a) and (b) Real and imaginary parts of the electric fields, respectively. (c) and (d) Real parts and imaginary parts of the magnetic fields, respectively.

$$\overline{\overline{\sigma}}_{s2} = \begin{bmatrix} 0.015 & 0 & 0 \\ 0 & 0.02 & 0 \\ 0 & 0 & 0.025 \end{bmatrix} \text{ S/m} \tag{42}$$

for the external cylindrical ring. The computation domains for both BCGS-FFT method and COMSOL simulation are the same as those in case 1. We also choose 10 PPW and 25 PPW for our BCGS-FFT solver. By placing a dipole source at $(0, -0.25, 0)$ m and a receiver array, including 40 receivers, at the $y = 0.25$ m plane, we obtain the total fields in the computation domain and the scattered fields at the receiver array. The z-component comparisons of the total fields solved by our BCGS-FFT method and COMSOL simulations are shown in Fig. 5, and the z-component comparisons of the scattered fields are shown in Fig. 6. Here, we also only pick 64 uniformly distributed sampling points inside the computation domain for the total field comparisons. We can see that the z-component of both the total fields and scattered fields by our BCGS-FFT method is in agreement with the COMSOL simulated results. It is obviously discernible from Figs. 5 and 6 that the accuracy of our BCGS-FFT results is higher when PPW $= 25$ than that when PPW $= 10$ if the COMSOL simulated results are treated as reference. In this case, our BCGS-FFT solver takes 62 s for PPW $= 10$ and 365 s for PPW $= 25$ for the whole calculation process, and the memory consumption is 1 GB for PPW $= 10$ and 11 GB for PPW $= 25$. COMSOL requires 3300 s and 93-GB memory on the same machine.

C. Two-Layered Biaxial Anisotropic Sphere

In the aforementioned two cases, the electrical size of the object is about 4λ, where λ is the smallest wavelength inside the anisotropic scatterers. A larger scatterer is proposed in this case. The object is a two-layered sphere with the inner radius $r_1 = 0.2$ m and outer radius $r_2 = 0.4$ m, as shown in Fig. 7. The permittivity tensors and permeability tensors are the same as (39) and (40) for the inner sphere object and (41) and (42) for outer sphere shell. Therefore,

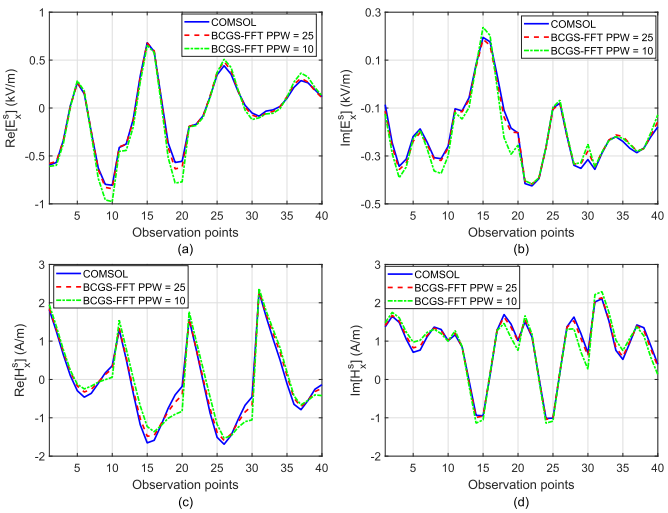

Fig. 6. z-component comparisons of the scattered fields at receiver array by the mixed-order BCGS-FFT and COMSOL. (a) and (b) Real and imaginary parts of the electric fields, respectively. (c) and (d) Real parts and imaginary parts of the magnetic fields, respectively.

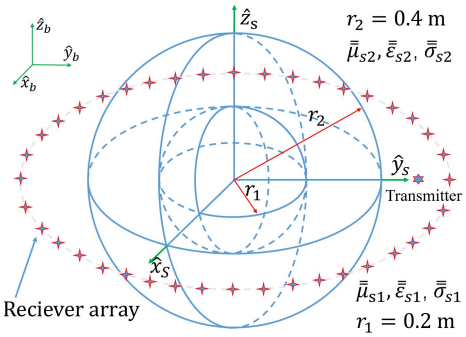

Fig. 7. Geometry of a two-layered sphere scatterer with the inner radius $r_1 = 0.2$ m and outer radius $r_2 = 0.4$ m.

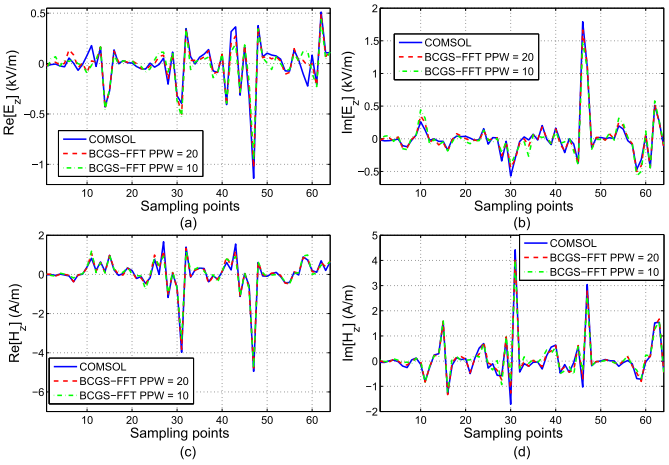

Fig. 8. z-component comparisons of the total fields for the two-layered sphere scatterer by the mixed-order BCGS-FFT and COMSOL. (a) and (b) Real and imaginary parts of the electric fields, respectively. (c) and (d) Real parts and imaginary parts of the magnetic fields, respectively.

the electrical size of the scatterer is about 8λ. The dipole source is placed at (0, 0.45, 0) m, and 40 receivers are placed in the $z = 0$ plane uniformly around the sphere object with

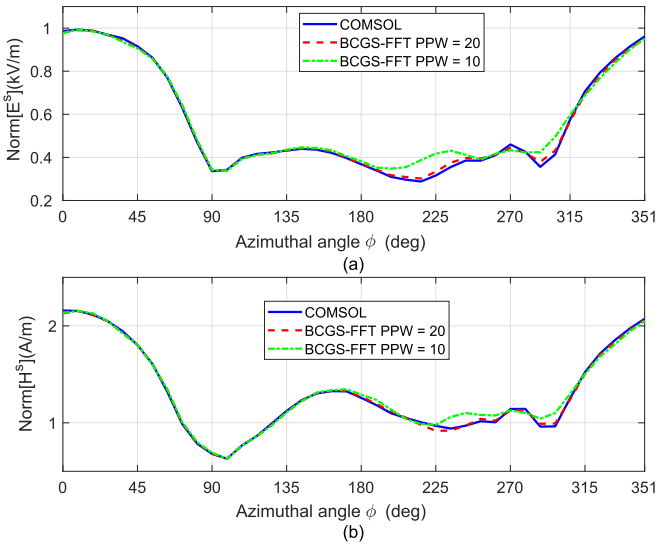

Fig. 9. Comparisons of the scattered field norms varying with the azimuthal angle ϕ for the two-layered cubic scatterer by the mixed-order BCGS-FFT and COMSOL. The transmitter is located at $\phi = 90°$. (a) Norms of the electric scattered fields. (b) Norms of the magnetic scattered fields.

the radius 0.5 m. The computation domain is a 0.8-m^3 cube, and it is discretized into 80^3 cells by 10 PPW and 160^3 cells by 20 PPW for the BCGS-FFT method, respectively. There are 3.072 million unknowns and 24.576 million unknowns for these two different discretization schemes. The computation domain of the COMSOL model is set as 1.1 m $\times$ 1.1 m $\times$ 1.0 m. The "User-controlled" option is used for the mesh size setting, and there are about 40.64 million unknowns. Fig. 8 shows z-component comparisons of total fields inside computation domain solved by our BCGS-FFT method and COMSOL simulations. Here, only 64 uniformly distributed sampling points inside the computation domain are picked for the total field comparisons. Obviously, the matching between our BCGS-FFT results and the COMSOL simulations is better when PPW = 20 than that when PPW = 10. Other components have similar agreements and are not shown here. The better performance for PPW = 20 of our BCGS-FFT method is further illustrated by the comparisons of the norms of scattered fields at the 40 receivers varying with the azimuthal angle ϕ, as shown in Fig. 9. The scattered fields are the strongest at the location $\phi = 0$ but weak near the transmitter or in its opposite side. This may be related to the source polarization and the two-layered sphere scattering. For the BCGS-FFT method, the total computation time is 398 s for PPW = 10 and 2998 s for PPW = 25. The memory consumption is 6.4 GB when PPW = 10 and 48 GB when PPW = 25. COMSOL requires 15 397 s and 380-GB memory on the same machine.

D. Optical Axis of the Scatterer Not Aligned With That of the Background Medium

In the aforementioned three cases, the principal axes of the magnetodielectric objects are aligned with the optical axis of the background medium, i.e., in the z-direction, in our computation. In this case, we suppose that the principal

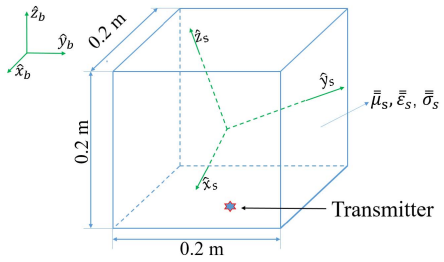

Fig. 10. Geometry of a cubic scatterer with the dimension of 0.2 m $\times$ 0.2 m $\times$ 0.2 m. The optical axis of the scatterer is not aligned with that of the background medium.

axis of the magnetodielectric object and the optical axis of the background medium are not aligned. It is assumed the optical axis of the object is in an arbitrary direction and can be aligned with that of the background medium after following three successive Euler rotations. The rotation angles are denoted as α, β, and γ, respectively. According to Euler's rotation theorem [46], the diagonal tensor of the object can be transformed into a new full tensor in the coordinate of the background medium by the Euler rotation matrix $R(\alpha, \beta, \gamma)$. The rotation equation can be written as

$$\overline{\overline{\eta}}_s' = R(\alpha, \beta, \gamma)\overline{\overline{\eta}}_s R^T(\alpha, \beta, \gamma) \tag{43}$$

where $\eta = \mu, \varepsilon, \sigma$. $\overline{\overline{\eta}}_s'$ is the full tensor after Euler's rotation, whereas $\overline{\overline{\eta}}_s$ is the diagonal tensor before the rotation. The subscript s represents the scatterer and the superscript T means the matrix transpose. The expression of the matrix R is given in Appendix B. In this case, we suppose the scatterer is a cube with the size of 0.2 m $\times$ 0.2 m $\times$ 0.2 m, as shown in Fig. 10. The permeability tensor, the permittivity tensor, and the conductivity tensor in the scatterer coordinates are

$$\overline{\overline{\mu}}_s = \mu_0 \begin{bmatrix} 2.0 & 0 & 0 \\ 0 & 1.5 & 0 \\ 0 & 0 & 3.0 \end{bmatrix} \quad \overline{\overline{\varepsilon}}_s = \varepsilon_0 \begin{bmatrix} 1.5 & 0 & 0 \\ 0 & 2.0 & 0 \\ 0 & 0 & 3.0 \end{bmatrix} \tag{44}$$

$$\overline{\overline{\sigma}}_s = \begin{bmatrix} 0.02 & 0 & 0 \\ 0 & 0.01 & 0 \\ 0 & 0 & 0.02 \end{bmatrix} \text{ S/m.} \tag{45}$$

We assume that the optical axis of the scatterer is aligned with that of the background medium after the Euler's rotation for $\alpha = 45°$, $\beta = 30°$, and $\gamma = 60°$, respectively. By substituting these angle values, (44), and (45) into (43), we obtain the new full magnetodielectric tensor that is applied to calculate the total field by our BCGS-FFT algorithm. The source is located at $(0, 0, -0.15)$ m. The computation domain has the same size as that of the scatterer. 10 PPW and 25 PPW are chosen to show the performance of our BCGS-FFT solver. The computation domain is discretized into 20^3 cells by 10 PPW and 50^3 cells by 25 PPW. In the COMSOL simulation model, the computation domain is 0.6 m $\times$ 0.6 m $\times$ 0.6 m which includes the electric dipole source, and the thickness of the PML is set as 0.1 m on the periphery of the computation domain. Fig. 11 shows the comparisons of the total fields inside the anisotropic object solved by our

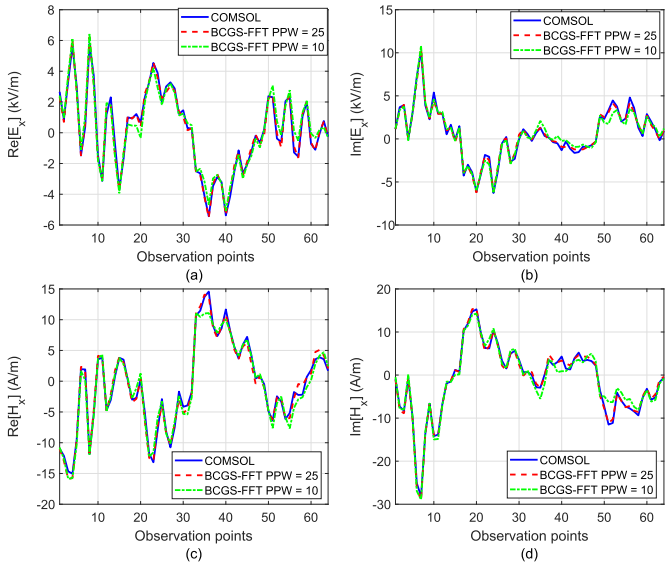

Fig. 11. x-component comparisons of the total fields inside the cubic scatterer by the mixed-order BCGS-FFT and COMSOL. The optical axis of the scatterer is not aligned with that of the background medium. (a) and (b) Real and imaginary parts of the electric fields, respectively. (c) and (d) Real and imaginary parts of the magnetic fields, respectively.

BCGS-FFT method and COMSOL simulations. We can see that the x-components of the total fields by our BCGS-FFT solver match the COMSOL simulated results well when PPW = 25. Other components also have the same good agreement but not shown here. In this case, the required time of the total calculation process is 18 s for PPW = 10 and 61 s for PPW = 25. The memory consumption is 200 MB for PPW = 10 and 1.8 GB for PPW = 25. COMSOL requires 1942 s and 105-GB memory on the same machine.

IV. Conclusion

In this paper, the BCGS-FFT algorithm is used to solve the discretized CFVIE formulated for the EM scattering of magnetodielectric objects embedded in a uniaxial background medium. The mixed-order as well as different types of basis functions are employed to expand flux densities and vector potentials in the CFVIE. The first-order volumetric rooftop basis functions are used for the flux densities to preserve the flux continuity in the element interface. The use of second-order curl conforming basis functions for the vector potentials can weaken the singularity of the CFVIE efficiently.

The performance of the proposed algorithm is validated by four numerical cases. Compared with the commercial software COMSOL, our BCGS-FFT algorithm is more than five times faster but consumes less than one-eighth memory. High computation accuracy is also validated by the comparisons between our BCGS-FFT numerical results and COMSOL simulations, and it is clear that higher accuracy is achieved by denser discretization scheme. The precise computed total fields and scattered fields for different shapes of the scatterers indicate that our method is suitable for scatterers with arbitrary shapes. Meanwhile, it is verified that the proposed VIE solver can handle scattering of anisotropic objects with large electrical sizes and arbitrary optical axes rotation embedded in uniaxial anisotropic media.

Appendix A

The expression of $\overline{\overline{\mathbf{G}}}_{\mathbf{EJ}}$ is given as [44]

$$\overline{\overline{\mathbf{G}}}_{\mathbf{EJ}}(\mathbf{r},\mathbf{r}') = \frac{1}{j\omega\epsilon_{xb}}\left[\nabla\nabla + k_{xb}^2\epsilon_{zb}\overline{\overline{\epsilon}}^{-1}\right]g_e(\mathbf{r},\mathbf{r}') + j\omega\mu_{xb}F(\mathbf{r},\mathbf{r}') \tag{46}$$

where

$$F(\mathbf{r},\mathbf{r}') = \left(\frac{\epsilon_{zb}}{\epsilon_{xb}}g_e - \frac{\mu_{zb}}{\mu_{xb}}g_m\right)f_1(\mathbf{r},\mathbf{r}') + \frac{r_e g_e - r_m g_m}{jk_{xb}\rho^2}f_2(\mathbf{r},\mathbf{r}') \tag{47}$$

$$g_e(\mathbf{r},\mathbf{r}') = \frac{e^{-jk_{xb}r_e}}{4\pi r_e} \quad r_e = \sqrt{\frac{\epsilon_{zb}}{\epsilon_{xb}}\rho^2 + (z-z')^2} \tag{48}$$

$$g_m(\mathbf{r},\mathbf{r}') = \frac{e^{-jk_{xb}r_m}}{4\pi r_m} \quad r_m = \sqrt{\frac{\mu_{zb}}{\mu_{xb}}\rho^2 + (z-z')^2} \tag{49}$$

$$k_{xb} = \sqrt{\omega^2\epsilon_{xb}\mu_{xb}} \tag{50}$$

$$\rho = \sqrt{(x-x')^2 + (y-y')^2} \tag{51}$$

$$f_1(\mathbf{r},\mathbf{r}') = \frac{1}{\rho^2}\begin{bmatrix} (y-y')^2 & -(x-x')(y-y') & 0 \\ -(x-x')(y-y') & (x-x')^2 & 0 \\ 0 & 0 & 0 \end{bmatrix} \tag{52}$$

$$f_2(\mathbf{r},\mathbf{r}') = \frac{1}{\rho^2} \times \begin{bmatrix} (x-x')^2-(y-y')^2 & 2(x-x')(y-y') & 0 \\ 2(x-x')(y-y') & (y-y')^2-(x-x')^2 & 0 \\ 0 & 0 & 0 \end{bmatrix}. \tag{53}$$

The expression of $\overline{\overline{\mathbf{G}}}_{\mathbf{HJ}}$ is given as [44]

$$\overline{\overline{\mathbf{G}}}_{\mathbf{HJ}}(\mathbf{r},\mathbf{r}') = \frac{(z-z')(g_e-g_m)}{\rho^2}f_3(\mathbf{r},\mathbf{r}') - (1+jk_{xb}r_m)\frac{\mu_{zb}g_m}{\mu_{xb}r_m^2}f_4(\mathbf{r},\mathbf{r}') + (1+jk_{xb}r_e)\frac{\epsilon_{zb}g_e}{\epsilon_{xb}r_e^2}f_4^T(\mathbf{r},\mathbf{r}') \tag{54}$$

where the superscript T means the matrix transpose, and

$$f_3(\mathbf{r},\mathbf{r}') = \begin{bmatrix} 2(x-x')(y-y') & (y-y')^2-(x-x')^2 & 0 \\ (y-y')^2-(x-x')^2 & -2(x-x')(y-y') & 0 \\ 0 & 0 & 0 \end{bmatrix} \tag{55}$$

$$f_4(\mathbf{r},\mathbf{r}') = \begin{bmatrix} \dfrac{(x-x')(y-y')(z-z')}{\rho^2} & \dfrac{-(x-x')^2(z-z')}{\rho^2} & 0 \\ \dfrac{(y-y')^2(z-z')}{\rho^2} & -\dfrac{(x-x')(y-y')(z-z')}{\rho^2} & 0 \\ -(y-y') & (x-x') & 0 \end{bmatrix}. \tag{56}$$

APPENDIX B

The expression for $R(\alpha, \beta, \gamma)$ is given as

$$R(\alpha, \beta, \gamma) = R(z, \alpha)R(y, \beta,)R(z, \gamma) \tag{57}$$

where $R(z, \alpha)$ means the rotation of an object by the angle α around the z-axis, $R(y, \beta)$ means the rotation of an object by the angle β around the y-axis, and $R(z, \gamma)$ means the rotation of an object by the angle γ around the z-axis. Their expressions are given as

$$R(z, \alpha) = \begin{bmatrix} \cos\alpha & -\sin\alpha & 0 \\ \sin\alpha & \cos\alpha & 0 \\ 0 & 0 & 1 \end{bmatrix} \tag{58}$$

$$R(y, \beta) = \begin{bmatrix} \cos\beta & 0 & \sin\alpha \\ 0 & 1 & 0 \\ -\sin\alpha & 0 & \cos\beta \end{bmatrix} \tag{59}$$

$$R(z, \gamma) = \begin{bmatrix} \cos\gamma & -\sin\gamma & 0 \\ \sin\gamma & \cos\gamma & 0 \\ 0 & 0 & 1 \end{bmatrix}. \tag{60}$$

REFERENCES

[1] B. E. A. Saleh, *Fundamentals of Photonics*, 2nd ed. Hoboken, NJ, USA: Wiley, 2007.

[2] Q. Ren, Q. Zhan, and Q. H. Liu, "An improved subdomain level nonconformal discontinuous Galerkin time domain (DGTD) method for materials with full-tensor constitutive parameters," *IEEE Photon. J.*, vol. 9, no. 2, Apr. 2017, Art. no. 2600113.

[3] D. M. Pozar, *Microwave Engineering*, 3rd ed. Hoboken, NJ, USA: Wiley, 2009.

[4] S. Mueller *et al.*, "Broad-band microwave characterization of liquid crystals using a temperature-controlled coaxial transmission line," *IEEE Trans. Microw. Theory Techn.*, vol. 53, no. 6, pp. 1937–1945, Jun. 2005.

[5] S. Müller, P. Scheele, C. Weil, M. Wittek, C. Hock, and R. Jakoby, "Tunable passive phase shifter for microwave applications using highly anisotropic liquid crystals," in *IEEE MTT-S Int. Microw. Symp. Dig.*, Jun. 2004, pp. 1153–1156.

[6] C. Fritzsch, S. Bildik, and R. Jakoby, "Ka-band frequency tunable patch antenna," in *Proc. IEEE Antennas Propag. Soc. Int. Symp.*, Jul. 2012, pp. 1–2.

[7] S. Mueller, M. Koeberle, A. Moessinger, F. Goelden, A. Gaebler, and R. Jakoby, "Liquid crystal based electronically steerable 4×4 antenna array with single horn feed at Ka-band," in *Proc. IEEE Antennas Propag. Soc. Int. Symp.*, Jul. 2008, pp. 1–4.

[8] S. Fakhte, H. Oraizi, L. Matekovits, and G. Dassano, "Cylindrical anisotropic dielectric resonator antenna with improved gain," *IEEE Trans. Antennas Propag.*, vol. 65, no. 3, pp. 1404–1409, Mar. 2017.

[9] F. D. Senghor, G. Wasselynck, H. K. Bui, S. Branchu, D. Trichet, and G. Berthiau, "Electrical conductivity tensor modeling of stratified woven-fabric carbon fiber reinforced polymer composite materials," *IEEE Trans. Magn.*, vol. 53, no. 6, Jun. 2017, Art. no. 9401604.

[10] D. Schurig *et al.*, "Metamaterial electromagnetic cloak at microwave frequencies," *Science*, vol. 314, no. 5801, pp. 977–980, 2006.

[11] S. Enoch, G. Tayeb, P. Sabouroux, N. Guérin, and P. Vincent, "A metamaterial for directive emission," *Phys. Rev. Lett.*, vol. 89, no. 21, p. 213902, 2002.

[12] P. Adamson, "Inverse relationships for ellipsometry of uniaxially anisotropic nanoscale dielectric films on isotropic materials," *Opt. Commun.*, vol. 285, nos. 13–14, pp. 3210–3216, Jun. 2012.

[13] Y. S. Cao, P. Li, L. J. Jiang, and A. E. Ruehli, "The derived equivalent circuit model for magnetized anisotropic graphene," *IEEE Trans. Antennas Propag.*, vol. 65, no. 2, pp. 948–953, Feb. 2017.

[14] K. Yang, J. C. Zhou, W. T. Sheng, Z. Y. Zhu, and M. S. Tong, "Efficient Nyström solutions of electromagnetic scattering by composite objects with inhomogeneous anisotropic media," *IEEE Trans. Antennas Propag.*, vol. 61, no. 10, pp. 5328–5332, Oct. 2013.

[15] Y. Jia, Z. He, A. Gholipour, and S. K. Warfield, "Single anisotropic 3-D MR image upsampling via overcomplete dictionary trained from in-plane high resolution slices," *IEEE J. Biomed. Health.*, vol. 20, no. 6, pp. 1552–1561, Nov. 2016.

[16] K. Sainath and F. L. Teixeira, "Spectral-domain computation of fields radiated by sources in non-birefringent anisotropic media," *IEEE Antennas Wireless Propagat. Lett.*, vol. 15, pp. 340–343, Jun. 2015.

[17] I. K. Ludlow and J. Everitt, "Inverse Mie problem," *J. Opt. Soc. Amer. A, Opt. Image Sci.*, vol. 17, no. 12, pp. 2229–2235, 2000.

[18] J. Yamamoto and T. Iwai, "Stability analysis of particle trapping in time-division optical tweezers by the generalized Lorentz-Mie theory," *Jpn. J. Appl. Phys.*, vol. 49, no. 49, pp. 092701-1–092701-6, 2010.

[19] R.-J. Tarento, K.-H. Bennemann, P. Joyes, and J. Van de Walle, "Mie scattering of magnetic spheres," *Phys. Rev. E, Stat. Phys. Plasmas Fluids Relat. Interdiscip. Top.*, vol. 69, no. 2, 2004, Art. no. 026606.

[20] K.-L. Wong and H.-T. Chen, "Electromagnetic scattering by a uniaxially anisotropic sphere," *Proc. Inst. Elect. Eng.—Microw., Antennas Propag.*, vol. 139, no. 4, pt. H, pp. 314–318, Aug. 1992.

[21] Y.-L. Geng, X.-B. Wu, L.-W. Li, and B.-R. Guan, "Mie scattering by a uniaxial anisotropic sphere," *Phys. Rev. E, Stat. Phys. Plasmas Fluids Relat. Interdiscip. Top.*, vol. 70, no. 5, 2004, Art. no. 056609.

[22] C. W. Qiu, S. Zouhdi, and A. Razek, "Modified spherical wave functions with anisotropy ratio: Application to the analysis of scattering by multilayered anisotropic shells," *IEEE Trans. Antennas Propag.*, vol. 55, no. 12, pp. 3515–3523, Dec. 2007.

[23] C.-W. Qiu, L.-W. Li, T.-S. Yeo, and S. Zouhdi, "Scattering by rotationally symmetric anisotropic spheres: Potential formulation and parametric studies," *Phys. Rev. E, Stat. Phys. Plasmas Fluids Relat. Interdiscip. Top.*, vol. 75, no. 2, Feb. 2007, Art. no. 026609.

[24] Y. L. Geng, C. W. Qiu, and N. Yuan, "Exact solution to electromagnetic scattering by an impedance sphere coated with a uniaxial anisotropic layer," *IEEE Trans. Antennas Propag.*, vol. 57, no. 2, pp. 572–576, Feb. 2009.

[25] L. Dou and A. R. Sebak, "3D FDTD method for arbitrary anisotropic materials," *Microw. Opt. Technol. Lett*, vol. 48, no. 10, pp. 2083–2090, Oct. 2010.

[26] H. Cai, B. Xiong, M. Han, and M. Zhdanov, "3D controlled-source electromagnetic modeling in anisotropic medium using edge-based finite element method," *Comput. Geosci.*, vol. 73, pp. 164–176, Dec. 2014.

[27] C. Forestiere, G. Miano, G. Rubinacci, A. Tamburrino, L. Udpa, and S. Ventre, "A frequency stable volume integral equation method for anisotropic scatterers," *IEEE Trans. Antennas Propag.*, vol. 65, no. 3, pp. 1224–1235, Mar. 2017.

[28] V. Sladek, J. Sladek, and C. Zhang, "Domain element local integral equation method for potential problems in anisotropic and functionally graded materials," *Comput. Mech.*, vol. 37, no. 1, pp. 78–85, 2005.

[29] A. Musolino, M. Raugi, and C. Visone, "A 3-D integral equation method for electromagnetic field analysis in anisotropic materials," *IEEE Trans. Magn.*, vol. 31, no. 3, pp. 1706–1709, May 1995.

[30] B. J. Zhu and T. Y. Qin, "Hypersingular integral equation method for a three-dimensional crack in anisotropic electro-magneto-elastic bimaterials," *Theor. Appl. Fract. Mech.*, vol. 47, no. 3, pp. 219–232, 2007.

[31] L. E. Sun and W. C. Chew, "A novel formulation of the volume integral equation for electromagnetic scattering," *Waves Random Complex Media*, vol. 19, no. 1, pp. 162–180, Feb. 2009.

[32] R. D. Graglia, P. L. E. Uslenghi, and R. S. Zich, "Moment method with isoparametric elements for three-dimensional anisotropic scatterers," *Proc. IEEE*, vol. 77, no. 5, pp. 750–760, May 1989.

[33] M. S. Tong and W. C. Chew, "Multilevel fast multipole algorithm for elastic wave scattering by large three-dimensional objects," *J. Comput. Phys.*, vol. 228, no. 3, pp. 921–932, Feb. 2009.

[34] P. Zwamborn and P. M. Van den Berg, "The three dimensional weak form of the conjugate gradient FFT method for solving scattering problems," *IEEE Trans. Microw. Theory Techn.*, vol. 40, no. 9, pp. 1757–1766, Sep. 1992.

[35] X. Nie, L.-W. Li, N. Yuan, and T. S. Yeo, "Fast analysis of scattering by arbitrarily shaped three-dimensional objects using the precorrected-FFT method," *Microw. Opt. Technol. Lett.*, vol. 34, no. 6, pp. 438–442, Sep. 2002.

[36] Z. Q. Zhang and Q. H. Liu, "Three-dimensional weak-form conjugate- and biconjugate-gradient FFT methods for volume integral equations," *Microw. Opt. Technol. Lett.*, vol. 29, no. 5, pp. 350–356, 2001.

[37] X. Millard and Q. H. Liu, "A fast volume integral equation solver for electromagnetic scattering from large inhomogeneous objects in planarly layered media," *IEEE Trans. Antennas Propag.*, vol. 51, no. 9, pp. 2393–2401, Sep. 2003.

[38] Z. Yu, W. Zhang, and Q. H. Liu, "A mixed-order stabilized bi-conjugate gradient FFT method for magnetodielectric objects," *IEEE Trans. Antennas Propag.*, vol. 62, no. 11, pp. 5647–5655, Nov. 2014.

[39] Z. Yu, W. Zhang, and Q. H. Liu, "The mixed-order BCGS-FFT method for the scattering of three-dimensional inhomogeneous anisotropic magnetodielectric objects," *IEEE Trans. Antennas Propag.*, vol. 63, no. 12, pp. 5709–5717, Dec. 2015.
[40] Y. Jia, Z. Yu, J. Dai, and Q. H. Liu, "Fast simulation of scattering problem for magnetodielectric materials with general anisotropy in layered media," *IEEE Trans. Antennas Propag.*, vol. 64, no. 11, pp. 4785–4793, Nov. 2016.
[41] Y. Zhong, P. P. Ding, M. Lambert, D. Lesselier, and X. Chen, "Fast calculation of scattering by 3-D inhomogeneities in uniaxial anisotropic multilayers," *IEEE Trans. Antennas Propag.*, vol. 62, no. 12, pp. 6365–6374, Dec. 2014.
[42] C. A. Balanis, Ed., *Advanced Engineering Electromagnetics*. New York, NY, USA: Wiley, 1989.
[43] W. C. Chew, "Vector potential electromagnetics with generalized gauge for inhomogeneous media: Formulation," *Prog. Electromagn. Res.*, vol. 149, pp. 69–84, Aug. 2014.
[44] W. S. Weiglhofer, "Dyadic Green's functions for general uniaxial media," *Proc. Inst. Elect. Eng.—Microw., Antennas Propag.*, vol. 137, no. 1, pt. H, pp. 5–10, Feb. 1990.
[45] J. Zhuo, F. Han, N. Liu, L. Ye, H. Liu, and Q. H. Liu, "Derivation and fast computation of dyadic Green's functions of magnetic vector potential for unbounded uniaxial anisotropic media," *Appl. Comput. Electromagn. Soc. J.*, vol. 32, no. 10, pp. 862–871, 2017.
[46] M. S. Khajeahsani, F. Mohajeri, and H. Abiri, "Rotational vector addition theorem and its effect on t-matrix," *IEEE Trans. Antennas Propag.*, vol. 59, no. 10, pp. 3819–3825, Oct. 2011.

Jianliang Zhuo received the B.S. degree in communication engineering and business administration and M.S. degree in communication and information system from the University of Electronic Science and Technology of China, Chengdu, China, in 2007 and 2011, respectively. He is currently pursuing the Ph.D. degree at Xiamen University, Xiamen, China.

His current research interests include fast-forward solvers in electromagnetics and inverse scattering methods for microelectronics and RF systems.

Feng Han (M'17) received the B.S. degree in electronic science from Beijing Normal University, Beijing, China, in 2003, the M.S. degree in geophysics from Peking University, Beijing, in 2006, and the Ph.D. degree in electrical engineering from Duke University, Durham, NC, USA, in 2011.

He is currently an Assistant Professor with the Institute of Electromagnetics and Acoustics, Xiamen University, Xiamen, China. His current research interests include ionosphere remote sensing by radio atmospherics, electromagnetic full-wave inversion by integral equations, reverse time migration image, and the design of electromagnetic detection systems.

Longfang Ye received the Ph.D. degree in electromagnetic field and microwave technology from the University of Electronic Science and Technology of China, Chengdu, China, in 2013.

From 2011 to 2013, he was a Visiting Student with the Massachusetts Institute of Technology, Cambridge, MA, USA. Since 2013, he has been an Assistant Professor with the Department of Electronic Science, Institute of Electromagnetics and Acoustics, Xiamen University, Xiamen, China. His current research interests include microwave circuits and antennas, terahertz waveguides, and graphene-based devices.

Zhiru Yu received the B.S. degree in electrical and information engineering and M.S. degree in electromagnetic fields and microwave technology from the University of Electronic Science and Technology of China, Chengdu, China, in 2007 and 2010, respectively, and the Ph.D. degree from Duke University, Durham, NC, USA.

From 2010 to 2015, he was a Research Assistant of computational electromagnetics with the Electrical and Computer Engineering Department, Duke University. His current research interests include frequency-domain methods for computational electromagnetics, inverse scattering for microelectronics and subsurface sensing, antennas, and RF systems.

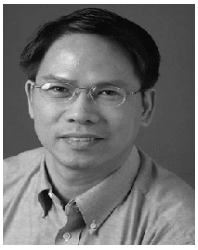

Qing Huo Liu (S'88–M'89–SM'94–F'05) received the B.S. and M.S. degrees in physics from Xiamen University, Xiamen, China, and the Ph.D. degree in electrical engineering from the University of Illinois at Urbana–Champaign, Champaign, IL, USA.

He was with the Electromagnetics Laboratory, University of Illinois at Urbana–Champaign, as a Research Assistant from 1986 to 1988 and as a Post-Doctoral Research Associate from 1989 to 1990. From 1990 to1995, he was a Research Scientist and the Program Leader with the Schlumberger-Doll Research Center, Ridgefield, CT, USA. From 1996 to 1999, he was an Associate Professor with New Mexico State University, Las Cruces, NM, USA. Since 1999, he has been with Duke University, Durham, NC, USA, where he is currently a Professor of electrical and computer engineering. He has authored or co-authored over 400 papers in refereed journals and 500 papers in conference proceedings. His current research interests include computational electromagnetics and acoustics, inverse problems, and their application in nanophotonics, geophysics, biomedical imaging, and electronic packaging.

Dr. Liu is a Fellow of the Acoustical Society of America, The Electromagnetics Academy, and the Optical Society of America. He was the recipient of the 1996 Presidential Early Career Award for Scientists and Engineers from The White House, the 1996 Early Career Research Award from the Environmental Protection Agency, the 1997 CAREER Award from the National Science Foundation, and the ACES Technical Achievement Award in 2017. He served as an IEEE Antennas and Propagation Society Distinguished Lecturer from 2014 to 2016. He is currently serving as the founding Editor-in-Chief of the IEEE JOURNAL ON MULTISCALE AND MULTIPHYSICS COMPUTATIONAL TECHNIQUES, the Deputy Editor-in-Chief of *Progress in Electromagnetics Research*, an Associate Editor of the IEEE TRANSACTIONS ON GEOSCIENCE AND REMOTE SENSING, and an Editor of the *Journal of Computational Acoustics*.